EPJ manuscript No.
(will be inserted by the editor)

Nanocomposites of magnetic cobalt nanoparticles and cellulose

K. Pirkkalainen[1], K. Leppänen[1], U. Vainio[2], M.A. Webb[2], T. Elbra[3], T. Kohout[3], A. Nykänen[4], J. Ruokolainen[4], N.E. Kotelnikova[5], and R. Serimaa[1]

[1] Division of Materials Physics, Department of Physics, P.O.B. 64, FI-00014 University of Helsinki, Finland
[2] Hamburger Synchrotronstrahlungslabor HASYLAB at DESY, Notkestrasse 85, D-22607 Hamburg, Germany
[3] Division of Atmospheric Sciences and Geophysics, Department of Physics, P.O.B. 64, FI-00014 University of Helsinki, Finland
[4] Laboratory of Optics and Molecular Materials, Helsinki University of Technology, P.O.B. 5100, FI-02015 TKK, Finland
[5] Institute of Macromolecular Compounds, Russian Academy of Sciences, Bolshoy pr. 31, St. Petersburg 199004, Russia

Received: date / Revised version: date

Abstract. Polymeric matrices with stabilized metallic nanoparticles constitute an important class of nanostructured materials, because polymer technology allows fabrication of components with various electronic, magnetic and mechanical properties. The porous cellulose matrix has been shown to be a useful support material for platinum, palladium, silver, copper and nickel nanoparticles. In the present study, nanosized cobalt particles with enhanced magnetic properties were made by chemical reduction within a microcrystalline cellulose (MCC) matrix. Two different chemical reducers, $NaBH_4$ and NaH_2PO_2, were used, and the so-formed nanoparticles were characterized with X-ray absorption spectroscopy, X-ray diffraction, scanning electron microscopy and transmission electron microscopy. These experimental techniques were used to gain insight into the effect of different synthesis routes on structural properties of the nanoparticles. Magnetic properties of the nanoparticles were studied using a vibrating sample magnetometer. Particles made via the $NaBH_4$ reduction were amorphous Co-B or Co oxide composites with diminished ferromagnetic behaviour and particles made via the NaH_2PO_2 reduction were well-ordered ferromagnetic hcp cobalt nanocrystals.

PACS. 61.05.cp X-ray diffraction – 82.35.Np Nanoparticles in polymers – 87.64.kd X-ray absorption spectroscopy: EXAFS, NEXAFS, XANES, etc.

1 Introduction

Magnetic nanoparticles have been the topic of a number of studies due to their applications e.g. in high-density magnetic recording devices or magnetic sensors [1]. The unique properties of nanoparticles are determined primarily by the fact that most of the atoms in the particle belong to its surface [2]. In addition, crystallinity, size distribution, shape of particles and proximity of neighbouring particles affect the response of material when a magnetic field is applied to it [3]. Naturally the chemical neighborhood of surface atoms affects electrical and magnetic properties of the particle and from this point of view the medium or matrix in which nanoparticles are embedded should have an essential influence on the properties of nanoparticles itself. Also, by dispersing nanoparticles into a matrix, the distance between neighbouring particles can be manipulated.

Polymeric matrices with stabilized magnetic nanoparticles constitute an important class of nanostructured materials, because polymer technology allows the fabrication of components with various electronic, magnetic and mechanical properties [3,4]. Porous supports for nanosized particles have been used to enhance the catalytic activity of metals and their oxides, and to control the growth and properties of nanoparticles. For example, nanosized Ag-particles have been produced by using starch biopolymer support, with size controlled growth of particles with size ranges from 10 to 30 nm [5]. Also, stable Ag-nanoparticles with very narrow size distributions have been produced in an agar-agar matrix [6]. Recently, there have been studies of living plants or bacteria as biological factories for synthesizing metallic nanoparticles. In the studies by Gardea-Torresdey *et al.*, metallophytes (i.e. metal tolerant plants) were used to make crystalline Au and Ag nanoparticles [7, 8]. Some bacteria are known to actively uptake and bioreduce metal ions from solutions and synthesize magnetic nanoparticles [9,10].

In addition, a multitude of different support materials have been invented and used, but the need for biodegradable, economic, and on the other hand, widely available materials for supports, is substantial. Natural polymers have been used as supports and stabilizers for biologically active compounds for decades [11]. The porous cellulose matrix has been described as a template for metal nanosized particles and it has been shown to be a useful support material for platinum, palladium, silver, copper and

nickel nanoparticles. In these cases the cellulose fibre surfaces affected the nanoparticle formation, and nucleation and growth seemed to occur at least partially at pores and crevices of the cellulose fibres.

Conventionally, the composites have been made mechanically by mixing metal nanoparticles into molten or dissolved polymer matrix. This method often leads to an inhomogenous dispersion of particles [1]. Thus considerable attention has been paid in the in situ chemical synthesis of metal nanoparticles in polymer matrices.

Over the last 40 years, borohydride (BH_4^-) reduction of metal ions has been used extensively for the formation of metallic particles. In 1979 Dragieva *et al.* [12] reported that amorphous transition-metal boron alloys can be produced by chemical reduction of aqueous solutions of transition metal salts with $NaBH_4$. Since that time, quite a number of studies have dealt with structural and magnetic properties of Co-B composite particles prepared by this technique. The effects of reaction conditions on nanosized particles in the borohydride reduction process were studied systematically by Glavee *et al.* [13,14]. According to their studies, the primary product of this reaction, when carried out in aqueous medium, are either nanosized Co_2B or $Co(BO_2)_2$ particles depending on the specific mixing procedures and product handling. However, when the same reaction was carried out in non-aqueous medium, primary products were metallic Co-particles.

The use of hypophosphite ($H_2PO_2^-$) reduction for making metallic nanoparticles is far less common, and the reduction process has not been systematically studied. Previously, NaH_2PO_2 has been used for making of nickel and nickel phosphate particles in inert conditions [15]. It was observed that particle size could be controlled through the ratio $H_2PO_2^-/Ni^{2+}$ so that small particles had a large phosphorus content and vice versa. The smallest particles were amorphous and 27 nm in diameter on the basis of transmission electron microscopy. Upon heating, crystalline phases of fcc Ni and tetragonal Ni_3P emerged. Quite similar results were acquired in our previous study [16], where nickel nanoparticles were chemically made, by using KH_2PO_2 as a reducer, inside a microcrystalline cellulose matrix. The resulting particles were amorphous Ni-P composites, with particle sizes ranging from few nanometres to much larger aggregates with sizes up to micrometre range.

Electron microscopy has been used extensively to study the morphology of magnetic transition metal nanoparticles. In the case of crystalline particles, crystal structure and average size of crystallites has been obtained with X-ray diffraction. In the case of non-crystalline or weakly ordered materials, X-ray absorption spectroscopy has been widely used to probe chemical neighborhood and coordination of atom species of interest [17]. The near-edge region of absorption spectrum gives information on oxidation and chemical bonding of transition metal atoms in the nanoparticles, as well as an estimation for mass fraction of studied atom species in the sample. In principle, the magnetic properties of samples can be correlated with the structure of nanoparticles.

Table 1. Samples numbered # and sample preparation parameters. Sample named 3b stands for the sample, which was used in transmission electron microscopy studies. In the used medium, (t) corresponds to tartrate- and (c) to citrate salt. Ratio is the molar ratio BH_4^-/Co^{2+} or correspondingly $H_2PO_2^-/Co^{2+}$. The mass% of Co in samples according to elemental analysis (el) and according to X-ray absorption (x). The uncertainty in values of x is about 0.5.

#	Medium	Reducer	Ratio	el	x
1	$NH_3{\cdot}H_2O$ (t)	$NaBH_4$	2	7.3	6.2
2	$NH_3{\cdot}H_2O$ (t)	$NaBH_4$	4	7.5	6.3
3	$CoSO_4 \cdot 7H_2O$ (t)	NaH_2PO_2	20	5.6	3.7
3b	$CoSO_4 \cdot 7H_2O$ (t)	NaH_2PO_2	20	8.8	5.2
4	$CoSO_4 \cdot 7H_2O$ (t)	NaH_2PO_2	40	13.3	7.8
5	$CoSO_4 \cdot 7H_2O$ (c)	NaH_2PO_2	20	6.2	5.4
6	$CoSO_4 \cdot 7H_2O$ (c)	NaH_2PO_2	20	7.2	6.7

In this work, X-ray absorption spectroscopy (XAS), wide-angle X-ray scattering (WAXS), electron microscopy in transmission and scanning modes (TEM and SEM) were used to study the structure and morphology of cobalt particles embedded in a cellulose matrix. The magnetic properties of samples were studied using a vibrating sample magnetometer (VSM).

2 Sample preparation

Cobalt nanoparticles were synthesized into a microcrystalline cellulose (MCC) matrix by diffusion of cobalt ions, Co^{2+}, from solutions of $Co(CH_3COO)_2 \cdot 4H_2O$ (Shostka Chemical Industry plant, Russia) or $CoSO_4 \cdot 7H_2O$ (Ural Chemical Industry plant, Russia) prepared in tartrate $K_2C_4H_4O_6 \cdot 0.5H_2O$ (Chemical-pharmaceutical plant, Moscow) and $NaC_4H_4O_6{\cdot}4H_2O$ (Vecton, Russia) or citrate $Na_3C_6H_5O_7{\cdot}5.5H_2O$ (Red chemist, Russia) salts, and subsequent reduction of Co^{2+}. The microcrystalline cellulose was prepared by mild acid hydrolysis and contained moisture less than 1 mass%.

After reduction the powders were isolated from the suspensions, thoroughly rinsed with water and ethanol, and dried in vacuum at 313 K. The resulting powders were colored light gray, gray or black. The samples selected for this study are listed in Table 1.

2.1 Reduction of Co^{2+} with sodium boronhydride $NaBH_4$

Diffusion of Co^{2+} to the MCC matrix was carried out under intensive stirring of 1 g of MCC in 20 ml (1 M) of ammonium hydrate ($NH_3{\cdot}H_2O$) and 2 ml (0.1 M) of $Co(CH_3COO)_2 \cdot 4H_2O$-tartrate salt solution for 1 h at 293 K. The $NH_3{\cdot}H_2O$ plays a role as an additional ligand of Co^{2+} ions and as a buffer for increasing pH value to 12.

The reduction of Co^{2+} was carried out by adding 20 ml solution of $NaBH_4$ to the obtained suspension and intensive stirring was continued for 15 to 60 minutes at 323 K. The concentration of $NaBH_4$ varied between 0.11 to 0.55 mol/l.

2.2 Reduction of Co^{2+} with sodium hypophosphite NaH_2PO_2

Diffusion of Co^{2+} to the MCC matrix was carried out under intensive stirring of 1 g of MCC in 20 ml of $CoSO_4 \cdot 7H_2O$-tartrate or $CoSO_4 \cdot 7H_2O$-citrate salt solution for 1 h at 293, 323 or 368 K.

The reduction of Co^{2+} was carried out by adding a mixture of 10 ml (6 M) solution of sodium hydroxide and 10 ml solution of $NaH_2PO_2 \cdot H_2O$ to the obtained suspension and intensive stirring was continued for 15 to 180 minutes at 368 K. The concentration of NaH_2PO_2 varied between 3 to 8 mol/l.

3 Methods

3.1 Scanning electron microscopy

The micrometre-scale structures of microcrystalline cellulose samples and those subjected to chemical treatment were studied by scanning electron microscopy using a Jeol JCM-35 CF (Jeol, UK) instrument. To obtain micrographs, the samples were preliminarily mounted on an aluminum support covered with a carbon layer in a special chamber, and then sputtered under inert gas using a gold target.

3.2 Transmission electron microscopy

Transmission electron microscopy (TEM) micrographs were obtained at the Helsinki University of Technology using a FEI Tecnai 12 TEM with a LaB_6 thermionic gun operating at 120 kV. The powder samples were moulded into Ebonite-12 epoxy. Then the epoxy-sample pieces were cut by Leica Ultracut ultramicrotome. Thickness of slices was 70 nm and they were placed on copper grids. Micrographs were taken using the bright field mode.

3.3 Wide-angle X-ray scattering

Wide-angle X-ray scattering measurements were carried out in perpendicular transmission geometry using Cu Kα_1 radiation. A setup with a Rigaku rotating anode (fine focus) X-ray tube and a MAR345 image plate detector was used. The beam was monochromated and focused to detector with a bent Si(111) crystal and a totally reflecting mirror. Samples were heated in situ under helium atmosphere with a Linkam heating stage. Heating was started at room temperature of 303 K, and temperature was raised to 323, 373, 423, 473, 523, 573, 623 and finally 673 K with a gradient of 10 K/min. After that the sample was cooled back to 303 K. After each temperature step, a 5 minute pause was kept to ensure an isotropic distribution of heat in the sample. In each temperature step the diffraction pattern was cumulated for 15 minutes. The intensities were corrected for absorption of radiation and a geometrical factor to compensate for flat detector. The angular range was calibrated with silver behenate and silicon standards. The useful q-range of detector was from 0.5 to 3.5 1/Å. The length of the scattering vector q is defined as $q = 4\pi \sin(\theta)/\lambda$, where θ is the Bragg angle and λ is the wavelength of the used radiation. Broadening of diffraction maxima due to instrument was determined to be 0.2° at 47°. The average size of crystallites, B_{hkl} was determined by using the Scherrer formula

$$B_{hkl} = \frac{0.9\lambda}{\sqrt{(\Delta 2\theta)^2_{hkl} - (\Delta 2\theta)^2_{inst}}\cos\theta_{hkl}}, \qquad (1)$$

where θ_{hkl} is the angle of hkl reflection, $(\Delta 2\theta)_{hkl}$ is the full width at half maximum (FWHM) of the diffraction maximum hkl in radians and $(\Delta 2\theta)_{inst}$ is instrumental broadening in radians [18]. In Eq. 1 shape of diffraction maximum is taken to be Gaussian.

The heating degraded the cellulose and for that reason the heated samples were not used again in any other experiments in this study.

3.4 X-ray absorption

The X-ray absorption measurements were conducted at experimental station X1 (Römö II) at HASYLAB, Hamburg. Absorption spectra of the samples were measured by three ionization chambers, which monitored beam intensity before and after the sample and a reference sample. Absorption spectra were measured around the cobalt K-absorption edge (7709 eV) with an energy range from 7509 eV to 8709 eV. A step-by-step energy scan was used and a typical scan took 1-2 hours. For optimal detector performance, ionization chambers were filled with Ar-gas with optimal gas pressures calculated with the XAFSmass [19] computer software. To remove effects such as the high absorption by air and the resulting high pass filtering of the X-ray beam, the sample was placed in a vacuum chamber. During the measurements, chamber air pressure was around 3×10^{-3} mbar.

The EXAFS (Extended X-ray Absorption Fine Structure) oscillations were acquired from measured absorption spectra using the Viper computer software [20]. FEFF 8.2 [21,22] was used to calculate theoretical oscillations of different cobalt structures. Viper was also used for k-space fitting.

Experimental data were reduced by standard data procedures in Viper. Background subtraction was done by fitting a third degree polynomial to pre-edge part of the spectrum and a smooth curve to atomic absorption part of the spectrum. Normalization was done by dividing the data by height of the edge step. Energy scale was transformed to wave number k-space and multiplied by factor

of k^3 or k^2. The phase shifted radial distribution function in r-space was obtained via Fourier transformation with a Gaussian-rounded ends window function. The main peak contribution to $\chi(k)$ was obtained by using a Hanning window function and back transforming over r space range $0.5 - 2.75$ Å for samples 3, 4, 5, 6, $0.5 - 3.20$ Å for sample 1 and $0.5 - 2.75$ Å for sample 2. A curve-fitting analysis was done first in k-space for the original $\chi(k)$, and the fitting result was then checked and adjusted for filtered oscillations. The fitting in Viper was done by using the basic single scattering EXAFS equation

$$\chi(k) = S_0^2 \sum_j \frac{N_j f_j(k)}{k r_j^2} \exp\left(-2\sigma_j^2 k^2\right) \sin\left(2kr_j + \delta_j(k)\right). \quad (2)$$

The sum is taken over coordination shells j of the absorbing atom. Interatomic distances r, coordination numbers N, Debye-Waller factors σ^2 and threshold energy shifts E_0 were kept as fitting parameters and different Co-Co, Co-O and Co-B near environments were fitted into the experimental data. Backscattering amplitudes $f(k)$ and phase shifts $\delta(k)$ for hcp Co, fcc Co, CoO, Co_3O_4 and Co_2B were simulated using FEFF8. The program ATOMS [23] and crystallographic data was used to generate the feff.inp files, which were used for simulation of EXAFS oscillations. FEFF8 generated a large number of scattering paths. Only few first scattering paths were used in Viper program, because Viper uses the EXAFS formula based on single-scattering approximation. Amplitude reduction factor S_0^2 was calculated by fitting to experimental Co-foil calibration sample data using both Viper and IFEFFIT programs [24].

In all cases many different fits were applied, and the fit, which gave the lowest value for the R-factor (normalized rms-difference between model and experimental curves), was chosen. For the samples, in which the reducer was NaH_2PO_2 (samples 3, 4, 5 and 6), best results were gained by fitting two Co-Co environments with slightly different distances. The fitting results corresponded very well with two first scattering shells of metallic hcp Co. In the case of hcp structure, 1st and 2nd coordination shells coincide with each other, so they can be regarded as one, hence the coordination number of this shell is the sum $N_1 + N_2$. Theoretical coordination number for bulk hcp structure is 12. For sample 1, the best fit was achieved by using one Co-O environment and three Co-Co environments with different distances. For sample 2, Co-B and Co-Co environments gave the best results.

The mass fraction of Co in the samples was extracted from unnormalized absorption $\mu(E)D$. Experimental intensity at pre-edge region and at after-edge region were fitted with straight lines in order to determine the edge jump. Theoretical edge jump in the mass absorption coefficient μ/ρ is about 300 $\mathrm{cm^2 g^{-1}}$ for Co K-edge [25]. The mass fraction of cobalt, w_{Co}, in samples were calculated as [26]

$$w_{Co} = \frac{A\Delta(\mu D)}{m_s \Delta(\mu/\rho)}, \quad (3)$$

where μ is the linear absorption coefficient, $\Delta(\mu D)$ is the measured edge jump, D is the sample thickness, and $\Delta(\mu/\rho)$ is the theoretical edge jump. Area of the sample is A and mass of the sample is m_s. Calculated mass fractions for cobalt in samples are shown in table 1.

X-ray absorption near edge structure (XANES) data were normalized by subtracting the line fitted to region below the edge and by fitting a line above the edge for which absorption was set to 1 at 7740 eV.

3.5 Magnetic properties

Magnetic properties of the samples were measured using a Princeton Measurements Corporation (PMC) Micromag model 3900 VSM (Vibrating Sample Magnetometer) at room temperature. About 10 - 30 mg of sample powder was used in one measurement. Magnetization values given in this study are normalized to mass of cobalt in the sample, determined with X-ray absorption method. Field strengths are given in Tesla and are thus multiplied by permeability of free space. Magnetic measurements were done at a very late stage of this study, so powders which constitute the samples were scarce. Only for samples 2, 4, 5 and 6 there was enough of the powder left for magnetic studies. Quite fortunately, in this group is at least one sample from each of the different synthesis routes.

4 Results and discussion

The micrometre-scale structure of all the samples was studied with SEM (Fig. 1). Spherical particles of various sizes were observed in pores or crevices on the surface of fibrous cellulose. In some cases, particles were merged together to form larger aggregates.

In addition, nanometre-scale structure of one of the samples prepared via NaH_2PO_2 reduction (sample 3b) was studied by TEM (Fig. 2). The nanometre-scale size distribution of nanoparticles, as shown in Fig. 3, was obtained from TEM micrograph. The size distribution of particles shows that the average size of the particles is about 7.4 nm. The smallest particles that can be seen in the figure are about 3 nm and the largest particles are about 14 nm. On the other hand, the small amount of particles seen in TEM micrograph make any qualitative results at best dubious due to statistical inaccuracy. Even so, the TEM results are presented as quantitative proof for the existence of nanometre sized particles.

4.1 Samples 1 and 2, prepared via the $NaBH_4$ reduction

X-ray diffraction measurements in room temperature were mostly inconclusive. Diffraction pattern from crystalline cellulose could be seen clearly in all the samples, but aside from that, there were no other well-defined diffraction maxima in the measured angular range. However, a very

faint and broad intensity distribution was found with at 3.06 1/Å. Diffraction patterns are shown in Fig. 4.

Heating of these samples did not produce any additional diffraction peaks arising from nanoparticles, however at temperatures between 573-623 K, cellulose in the samples degraded and the respective diffraction pattern vanished. Also, the diffraction maxima shifted to slightly higher values due to thermal expansion of lattice planes. The anomalous faint maxima at 3.06 1/Å retained its form through the heating process, and can thus be linked to particles themselves with a certainty. However, the low signal-to-noise ratio of the respective maximum inhibited any detailed analysis. The faint maximum is assumed to arise from a disordered cobalt phase.

The absolute of Fourier transform (FT) of measured EXAFS k-space oscillations multiplied by different k-weights, $|\mathrm{FT}\{k^n\chi(k)\}|$, is shown in Fig. 8. As can be seen from the figure, the relative intensities of different peaks are modified with different k-weights. This is often a consequence of more than one constituent atomic species in the sample, to be more specific, the existence of heavy elements (cobalt) and light elements (oxygen, as an educated guess). It is well known that if intensity of a peak increases with the growing k-weight, the peak arises from the heavier element [27]. This effect is due to difference in backscattering amplitudes $f(k)$ of atoms of different species. As a result, the particles of samples 1 and 2 are assumed to be composites of cobalt and some significantly lighter element, such as oxygen or boron.

Measured EXAFS k-space oscillations of the samples were fitted with coordination shells from two possible crystal phases of cobalt, namely the fcc and hcp crystal structures of cobalt. None of these models corresponded well to measured k-space oscillations. Near-edge region of absorption spectra (Fig. 7) suggested the existence of a non-trivial chemical neighborhood for cobalt atoms, for the "white line" right before or after absorption edge and energy shift of the edge are often related to changes in the formal chemical valence of studied atom species [28,17], and thus Co-O environments were also tested. In addition, due to earlier studies by Glavee *et al.* [13,14] concerning the chemical making of nanoparticles via borohydride reduction, Co-B and Co-Co environments corresponding to shells from Co_2B were also fitted to measured EXAFS oscillations. One of the most consistent k-space fits are shown in Fig. 12. The original non-filtered oscillations are shown in Fig. 13. For sample 1, the best fit was acquired by using Co-O environment and Co-Co environments with three different distances (Table 2). For sample 2, the best fit was acquired by using Co-B and Co-Co environments (Table 2).

Magnetic hysteresis curves for the samples are shown in Fig. 14. Values for saturation M_s, coercivity H_c and remanent magnetization M_r were extracted from the measured hysteresis curves and the coercivity of remanence H_{cr} was determined from the backfield demagnetization (Table 4). Of all the samples included in the measurements of magnetic properties (see Sec. 3.5), sample 2 had the lowest values for saturation magnetization, which was more

Table 2. EXAFS fit parameters for samples 1 and 2 for all fitted shells. Parameter r is coordination shell distance from the central atom, N is coordination number and σ^2 is the Debye-Waller factor. The R-factor (normalized rms-difference between model and experimental curves) was 6.83 % for sample 1 and 4.84 % for sample 2. Fitted Co-environment is given in the first row.

Sample 1	Co-O	Co-Co	Co-Co	Co-Co
r (Å)	1.94	2.94	2.56	2.50
N	3.33	11.3	2.31	6.00
σ^2	0.016	0.018	0.004	0.009
Sample 2	**Co-B**	**Co-Co**	**Co-Co**	
r (Å)	2.05	2.50	2.62	
N	2.67	4.33	4.18	
σ^2	0.009	0.011	0.017	

or less half of the value acquired for samples made via NaH_2PO_2 reduction. One explanation for this is oxidation of the respective sample, for it has been shown in many cases that metal oxides have reduced magnetic activity compared to pure metals of the same atomic species [29], mostly due to antiferromagnetic or ferrimagnetic nature of these materials. On the other hand, surface oxidation of transition metal particles leads to a core-shell structure which can have a beneficial effect on the magnetic properties. If the core of the particle is metallic (ferromagnetic) and the shell is composed of metal oxides (antiferromagnetic), the interfacial coupling between core and shell is known to increase coercivity and remanence, but reduce saturation magnetization due to loss of net moment in the antiferromagnetic oxide shell. Oxide shells generally have small, on the order of few nanometres, crystallites which allows them to remain undetected in most X-ray diffraction measurements [3]. Thus a signal in our diffraction apparatus from such small crystallites would have been negligible. However, this does not seem to be the case in sample 2, for coercivity and remanence have much lower values than in the other measured samples. These results rule out the possibility of a metal-oxide core-shell structure and promote the existence of metal oxide particles.

Diminished ferromagnetic behaviour can be explained by disorder in the ferromagnetic phase. A disordered, and at least partly oxidized cobalt phase is very likely according to our results. It is also in complete agreement with previous studies in the chemical making of metal particles with $NaBH_4$ reduction [3,12–14,16].

According to the results, made particles are amorphous and are most likely composed of Co-B or Co oxide.

4.2 Samples 3, 4, 5 and 6, prepared via the NaH_2PO_2 reduction

X-ray diffraction measurements in room temperature showed three distinct diffraction maxima in addition to characteristic diffraction pattern of MCC (Fig. 5). Positions of the respective maxima were found to be at (2.91 ± 0.03),

Table 3. EXAFS fit parameters for samples 3,4,5 and 6. Number of the sample and goodness of the respective fit as a R-factor are given in the first row. In second row is the fitted Co-environment. Parameter r is coordination shell distance from the central atom, N is coordination number and σ^2 is the Debye-Waller factor.

	Sample 3	$R = 7.63$ %	Sample 4	$R = 5.45$ %
	Co-Co	Co-Co	Co-Co	Co-Co
r (Å)	2.45	2.54	2.46	2.50
N	6.23	4.93	3.73	5.81
N_1+N_2	11.2		9.54	
σ^2	0.0046	0.0037	0.0102	0.0067
	Sample 5	$R = 8.06$ %	Sample 6	$R = 6.82$ %
	Co-Co	Co-Co	Co-Co	Co-Co
r (Å)	2.45	2.51	2.45	2.52
N	4.57	5.81	7.98	3.45
N_1+N_2	10.4		11.4	
σ^2	0.0064	0.0072	0.0079	0.0052

Table 4. Magnetic properties of samples 2, 4, 5 and 6. M_r [Am^2/kg] is remanent magnetization, M_s [Am^2/kg] is saturation magnetization, H_{cr} [mT] is coercivity of remanence, and H_c [mT] coercivity. M_r and M_s are normalized by cobalt mass fractions acquired from X-ray absorption method. Due to uncertainties in exact determination of mass % of Co in the samples, there is an uncertainty of about ± 15 Am^2/kg in saturation values M_s.

#	M_r	M_s	H_{cr}	H_c	$\frac{M_r}{M_s}$	$\frac{H_{cr}}{H_c}$
2	4.77	67.8	28.9	7.52	0.07	3.84
4	25.0	165.8	44.7	23.9	0.15	1.88
5	10.8	91.8	54.7	15.9	0.12	3.43
6	15.7	111.9	90.3	27.9	0.14	3.23

(3.11 ± 0.03) and (3.27 ± 0.03) 1/Å, and they were indexed as 100, 002 and 101 reflections of hcp cobalt. Heating of the samples produced no changes in diffraction patterns, aside from the fact that cellulose degraded at temperature between 573-623 K and the respective diffraction pattern vanished. Both diffraction maxima from cellulose and hcp cobalt shifted to slightly higher values as a function of temperature, and this can be attributed to thermal expansion of the respective crystal lattices. The average size of crystallites was estimated with the Scherrer equation (Eq. 1). The average size of crystallites B_{101} as a function of temperature is visualized in Fig. 6. Although in general the average crystallite size for samples 3, 3b, 4 and 5 was about 6 nm, sample 6 seemed to have crystallites with more than twice that size. Upon heating, the crystallite sizes for samples 3, 3b, 4 and 5 increased somewhat, which is an indication of increased crystal order due to heating. Again sample 6 proved controversial as heating produced a slight reduction in the crystallite size.

Absolute of Fourier transform (FT) of measured EXAFS k-space oscillations multiplied by different k-weights, $|\mathrm{FT}\{k^n\chi(k)\}|$, is shown in Fig. 9. As can be seen from the figure, the relative intensities of different peaks remain the same with different k-weights. This is often the case when only one atomic species dominates in composition of the sample. As an approximation, particles in samples 3, 3b, 4, 5 and 6 are thus assumed to consist of only one atomic species. Near-edge region of absorption spectra (Fig. 7) for these samples show a very close resemblance to the spectrum measured from the cobalt foil calibration sample. This indicates that cobalt atoms in these samples are on average in a chemical neighbourhood similar to cobalt atoms in a bulk sample.

Measured EXAFS k-space oscillations were fitted with coordination shells from several possible crystal phases of cobalt, namely fcc and hcp crystal structures of cobalt, and in addition some oxides of cobalt. The more exotic cobalt variants, e.g. the epsilon and forced bcc crystal structures, were not included in this study due to their very rare occurences. The most consistent fits were gained with hcp cobalt. Fitted k-space oscillations are shown in Fig. 10 and the corresponding r-space fit in Fig. 11. The fitting parameters are given in Table 3. Coordination numbers, Debye-Waller factors and coordination shell distances were more or less the same that would be expected in well-ordered cobalt crystals.

Magnetic hysteresis curves for the samples are shown in Fig. 14. Values for saturation M_s, coercivity H_c and remanent magnetization M_r were extracted from measured hysteresis curves and the coercivity of remanence H_{cr} was determined from the backfield demagnetization. According to hysteresis curves, the samples made via NaH_2PO_2 reduction are clearly ferromagnetic. Saturation magnetization values were lower and coercivity values were higher than the respective values for bulk metallic cobalt. High values for coercivity in these samples suggest the existence of magnetic single domain nanoparticles. In single domain ferromagnetic particles, the changes in magnetization can no longer occur through domain wall motion but instead require coherent rotation of spins, therefore resulting in larger coercivities.

According to the results, the made particles are well-ordered hcp cobalt nanocrystals with particle sizes in nanometre regime. However, there are also much larger cobalt aggregates with sizes in micrometre range, although the particle size distribution appears to be dominated by the smaller, nanometre sized particles. Magnetic properties of the samples show that the smaller particles are single domain.

5 Conclusions

Cellulose was succesfully used as a support for amorphous and crystalline cobalt nanoparticles. Chemical synthesis route affected the coordination of Co atoms, the composition of nanoparticles and therefore also the magnetic properties. In the samples prepared with reducer $NaBH_4$, the nanoparticles were disordered and composed of Co, B and O. Magnetic properties were clearly diminished compared to bulk cobalt.

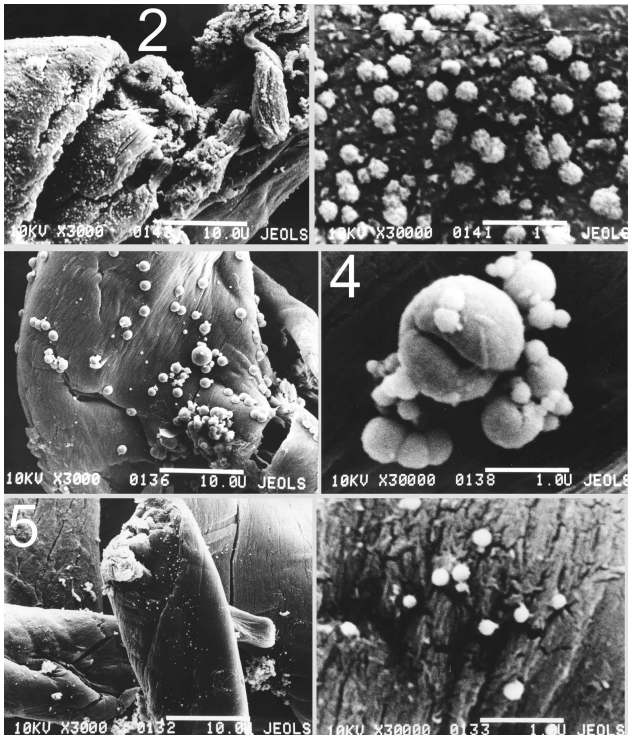

Fig. 1. SEM results for samples 2, 4 and 5 showing the micrometre-scale structure. White spheres contain cobalt and surrounding matrix is microcrystalline cellulose. On left the scale bars are 10 μm in length. On right is a 10 fold magnification with scale bars of 1 μm in length.

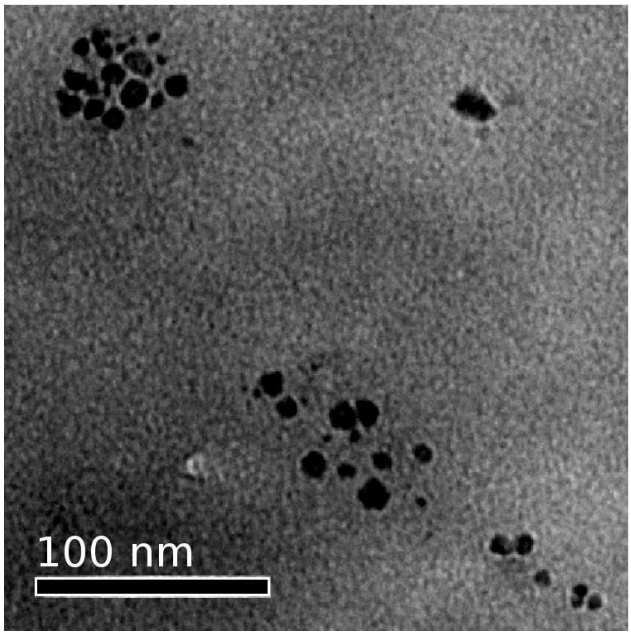

Fig. 2. TEM micrograph of sample 3b showing the nanometre-scale structure. Black spheres contain cobalt and surrounding matrix is microcrystalline cellulose. Scale bar is 100 nm in length.

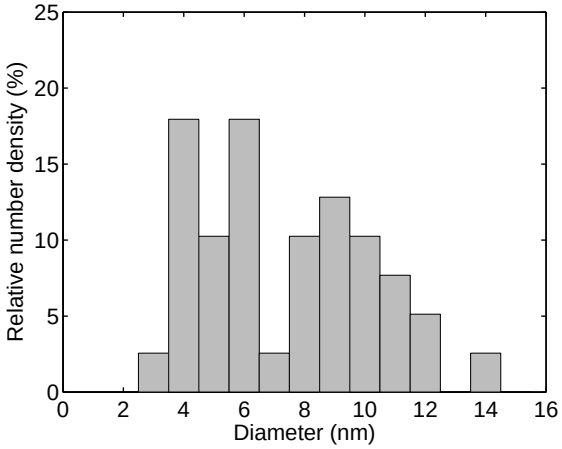

Fig. 3. Nanometre-scale size distribution for nanoparticles as obtained from TEM results of Fig. 2.

In the samples prepared with reducer NaH_2PO_2, the nanoparticles were well-ordered hcp nanocrystals with average crystallite sizes ranging from 5.3 to 6.3 nm and small amounts of larger aggregates in micrometre range. Magnetic properties of samples were near values reported for bulk cobalt. However, saturation magnetization was lower while coercivity was higher, which can be explained by the existence of particles with single magnetic domains.

According to X-ray diffraction, crystalline arrangement of cellulose matrix did not change due to chemical processing and intercalation of the nanoparticles.

We thank the HASYLAB organization for the possibility to conduct the X-ray absorption measurements. The Finnish national graduate school of nanosciences is acknowledged for financial support.

References

1. A. Sarkar, S. Kapoor, G. Yashwant, H.G. Salunke, T. Murkherjee, J. Phys. Chem. **109**, (2005) 7203-7207.
2. G.Y. Yurkov, D.A. Baranov, I.P. Dotsenko, S.P. Gubin, Composites: part B **37**, (2006) 413-417.
3. D.L. Leslie-Pelecky, R.D. Rieke, Chem. Mater. **8**, (1996) 1770-1783.
4. G. Schmid, Chem. Rev. **92**, (1992) 1709-1727.
5. D.K. Bozanic, V. Djokovic, J. Blanusa, P.S. Nair, M.K. Georges, T. Radhakrishnan, Eur. Phys. J. E **22**, (2007) 51-59.
6. E. Muthuswamy, S.S. Ramadevi, H.N. Vasan, C. Garcia, L. Noe, M. Verelst, J. Nanopart. Res. **9**, (2007) 561-567.
7. J.L. Gardea-Torresdey, J.G. Parsons, E. Gomez, J.R. Peralta-Videa, H.E. Troiani, P. Santiago, M. Jose-Yacaman, Nano Lett. **2**, (2002) 397-401.
8. J.L. Gardea-Torresdey, E. Gomez, J.R. Peralta-Videa, J.G. Parsons, H.E. Troiani, M. Jose-Yacaman, Langmuir **19**, (2003) 1357-1361.
9. D.R. Lovley, J.F. Stolz, G.L. Nord, E.J.P. Phillips, Nature **330**, 252-254.
10. D.P.E. Dickson, J. Magn. Mater **203**, (1999) 46-49.
11. U. Vainio, K. Pirkkalainen, K. Kisko, G. Goerigk, N.E. Kotelnikova, R. Serimaa, Eur. Phys. J. D **42**, (2007) 93-101.
12. I. Dragieva, G. Gavrilov, D.Buchkov, M. Slavcheva, J. Less-Comm. Met. **67**, (1979) 375-379.

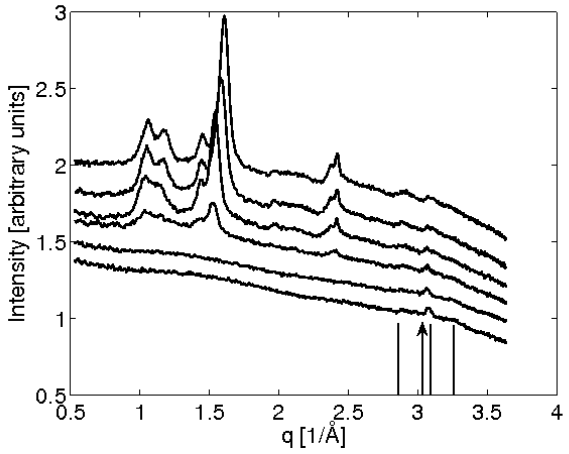

Fig. 4. Results of WAXS measurement with heating for sample 1 measured in temperatures top down 323, 423, 573, 623, 673 K and cooled back to 303 K. As can be seen, the reflections from cellulose disappear in highest temperature. Three vertical lines indicate theoretical positions of three strongest hcp-cobalt reflections 100, 002 and 101 and vertical arrow indicates the position of the strongest fcc-cobalt reflection 111.

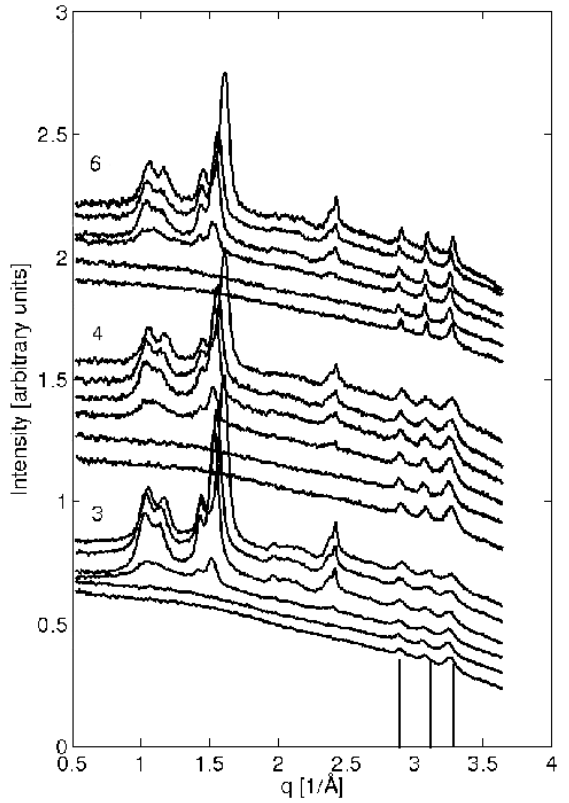

Fig. 5. Results of WAXS measurements with heating for the samples 3, 4 and 6. The intensities were measured in temperatures top down 323, 423, 573, 623, 673 K and cooled back to 303 K. Three vertical lines indicate theoretical positions of three strongest hcp-cobalt reflections 100, 002 and 101.

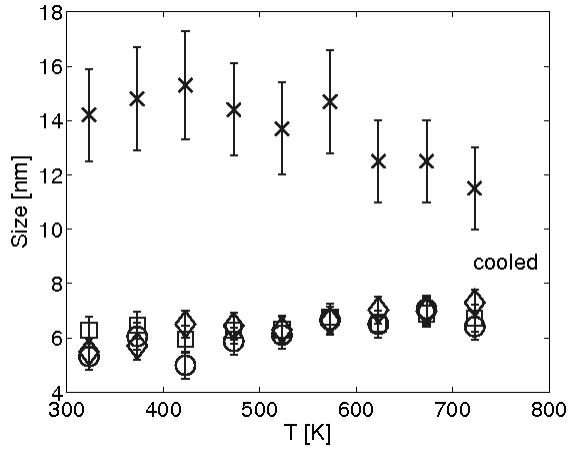

Fig. 6. Average sizes of cobalt crystallites in the samples 3 (diamonds), 4 (squares), 5 (circles) and 6 (x) as a function of temperature. Highest measurement temperature was 673 K and last points in the figures correspond to cooled state.

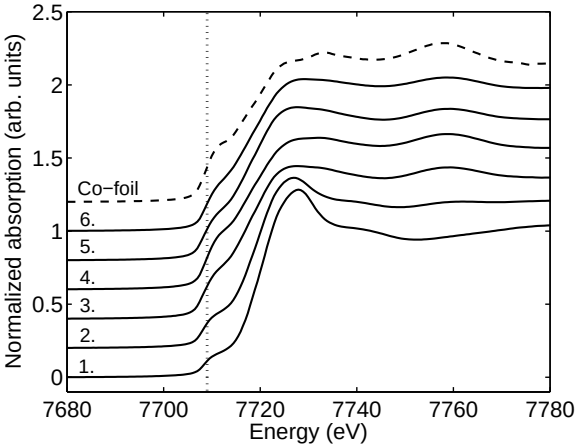

Fig. 7. Normalized XANES spectra of the samples (solid lines) and a Co foil (dashed line) calibration sample. Curves are shifted vertically for clarity. Vertical dotted line is drawn at the first inflection point of the spectrum of Co foil. Numbers above each curve correspond to the sample number.

13. G.N. Glavee, K.J. Klabunde, C.M. Sorensen, G.C. Hadjipanayis, Langmuir **8**, (1992) 771-773.
14. G.N. Glavee, K.J. Klabunde, C.M. Sorensen, G.C. Hadjipanayis, Inorg. Chem **32**, (1993) 474-477.
15. S. Xie, M. Qiao, W. Zhou, G. Luo, H. He, K. Fan, T. Zhao, W. Yuan, J. Phys. Chem. B **109**, (2005) 24361-24368.
16. K. Pirkkalainen, U. Vainio, K. Kisko, T. Elbra, T. Kohout, N.E. Kotelnikova, R. Serimaa, J. Appl. Cryst. **40**, (2007) S489-S494.
17. H. Modrow, Appl. Spectrosc. Rev. **39**, (2004) 183-290.
18. A. Guinier, *X-ray diffraction. In crystals, imperfect crystals, and amorphous bodies* (Dover publications, Inc., New York 1994), chapters 4.7, 5.
19. K.V. Klementiev, XAFSmass, freeware: www.desy.de/∼klmn/xafsmass.html
20. K.V. Klementiev, VIPER for Windows, freeware: www.desy.de/∼klmn/viper.html; K.V. Klementiev, J. Phys.

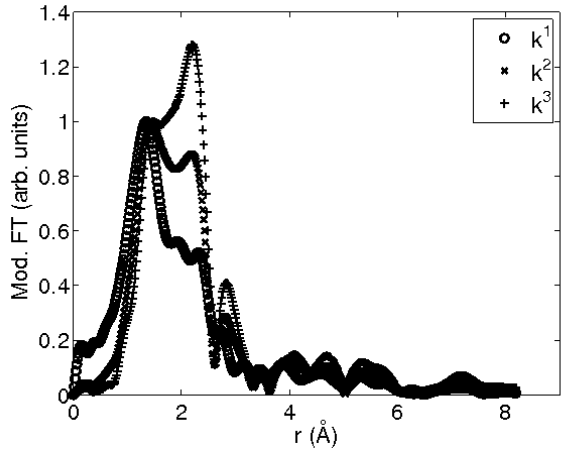

Fig. 8. Absolute values of Fourier transformation of EXAFS-spectrum for the sample 1 weighted with three different powers of k. Strong changes appear in heights of the peaks.

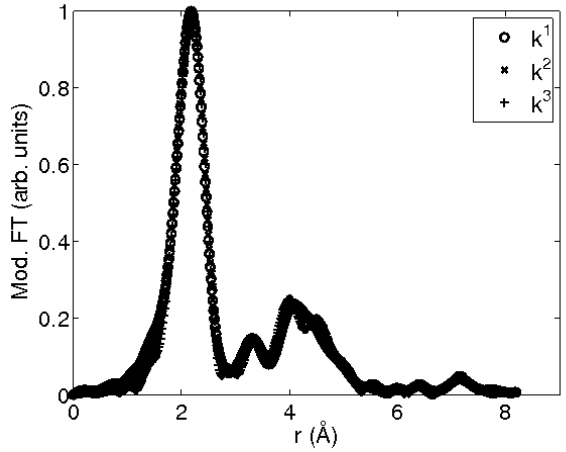

Fig. 9. Absolute values of Fourier transformation of EXAFS-spectrum for the sample 3 weighted with three different powers of k. Nearly no changes appear in heights of the peaks.

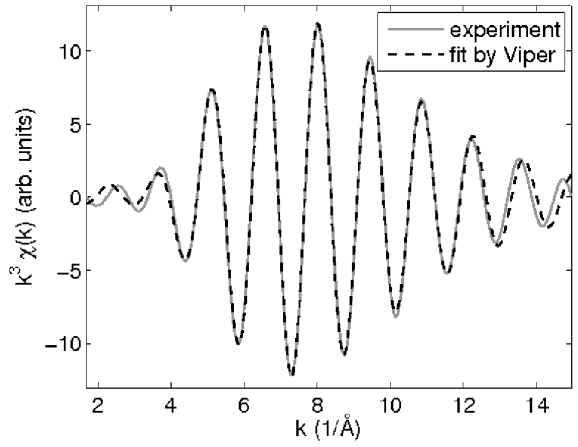

Fig. 10. Filtered EXAFS-spectrum (solid line) and k-space fitting result (dashed line) of sample 4.

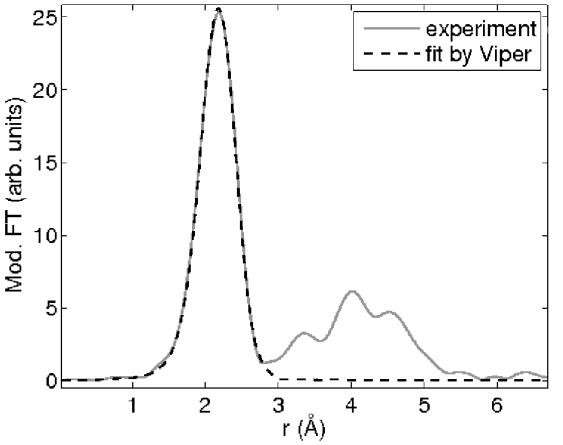

Fig. 11. Pseudo-radial distribution function of EXAFS-spectrum (solid line) and r-space fitting result (dashed line) of sample 4.

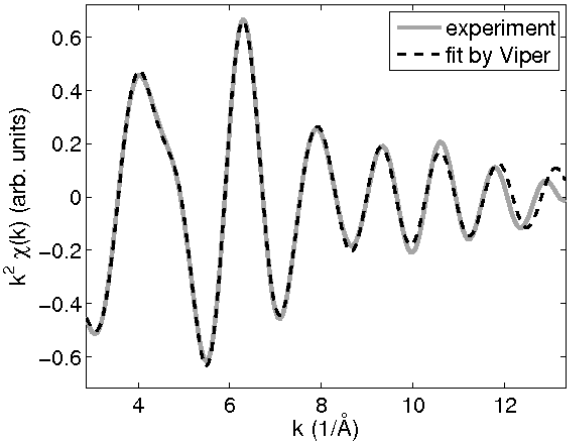

Fig. 12. Filtered EXAFS-spectrum (solid line) and k-space fitting result (dashed line) of sample 1.

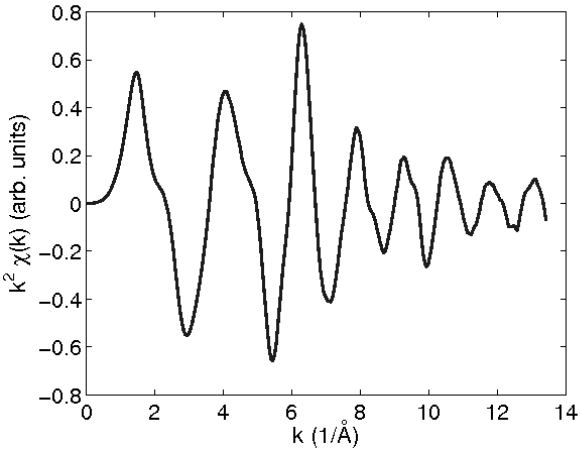

Fig. 13. Original $\chi(k)$ oscillations of sample 1.

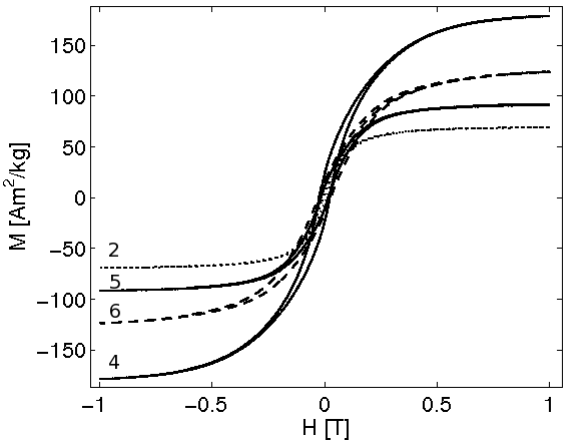

Fig. 14. Hysteresis loops measured for samples 2, 4, 5 and 6. Magnetization values are normalized by mass of cobalt in the samples as determined from X-ray absorption measurements.

D: Appl. Phys. **34**, (2001) 209-217.
21. S.I. Zabinsky, J.J. Rehr, A. Ankudinov, R.C. Albers, M.J. Eller, Phys. Rev. B **52**, (1995) 2995-3009.
22. A.L. Ankudinov, B. Ravel, J.J. Rehr, S.D. Conradson, Phys. Rev. B **58**, (1998) 7565-7576.
23. B. Ravel, J. Synchrotron Rad. **8**, (2001) 314-316.
24. M. Newville, J. Synchrotron Rad., **8**, (2001) 322-324.
25. C.T. Chantler, K. Olsen, R.A. Dragoset, A.R. Kishore, S.A. Kotochigova, D.S. Zucker. X-ray form factor, attenuation and scattering tables (version 2.1). National Institute of Standards and Technology, Gaithersburg, MD. Originally published as C.T Chantler, J. Phys. Chem. Ref. Data **29**, (2000) 597-1048; and C.T. Chantler, J. Phys. Chem. Ref. Data **24**, (1995) 71-643.
26. T. Vad, F. Hajbolouri, H.G. Haubold, G.G. Scherer, A. Wokaun, J. Phys. Chem. B **108**, (2004) 12442-12449.
27. D.C. Koningsberg, B.L. Mojet, G.E. van Dorssen, D.E. Ramaker, Topics in Catalysis **10**, (2000) 143-155.
28. G. Cheng, J.D. Carter, T. Guo, Chem. Phys. Lett. **400**, (2004) 122-127.
29. M.J. Aus, C. Cheung, B. Szpunar, U. Erb, J. Szpunar, J. Mat. Sci. Lett. **17**, (1998) 1949-1952.